Journal of the Korean Physical Society, Vol. 43, No. 4, October 2003, pp. 565∼573

Detectability Test of H_2 Lyman-Werner Band Emission for a Far-Ultraviolet Imaging Spectrograph FIMS

Kwang-Il Seon,* Soojong Pak, Jang-Hyun Park, In-Soo Yuk, Ho Jin, Uk-Won Nam and Wonyong Han
Korea Astronomy Observatory, Daejeon 305-348

Kwang-Sun Ryu, Dae-Hee Lee and Seung-Han Oh
Satellite Technology Research Center, Korea Advanced Institute of Science and Technology, Daejeon 305-701

Yong-Sun Park
Astronomy Program, School of Earth and Environmental Science, Seoul National University, Seoul 151-742

Eric J. Korpela, Jerry Edelstein and Kaori Nishikida
Space Sciences Laboratory, University of California, Berkeley, CA 94720-7450, U.S.A.

Jong-Ho Shinn, Jin-Gheun Rhee and Kyoung-Wook Min
Deptment of Physics, Korea Advanced Institute of Science and Technology, Daejeon 305-701

Yong-Ha Kim
Deptment of Astronomy and Space Science, Chungnam National University, Daejeon 305-764

(Received 21 May 2003)

Molecular hydrogen (H_2) is excited by far-ultraviolet (far-UV) photons and emits fluorescent emission in the far-UV bands and in the near- and the mid-infrared bands. Observations of H_2 in these photodissociation regions (PDRs) are important in tracing star-forming molecular clouds and in understanding the interaction between newly born stars and molecular clouds. We use the typical PDR model of Sternberg to estimate the observing time (or integration time) required to detect PDRs with the Far-ultraviolet IMaging spectrograph (FIMS) onboard KAISTSAT-4, the first Korean scientific satellite. The observing time is calculated using a formula based on a rigorous hypothesis testing for the detection limit, in contract to the often-used signal-to-noise ratio. The estimated observing time is also compared with the expected exposure time from one-year all-sky survey.

PACS numbers: 95.55.Fw, 95.85.Mt, 97.10.Bt
Keywords: Space-based ultraviolet telescopes, Ultraviolet, Star formation

I. INTRODUCTION

Molecular clouds are the birthplace of stars, and the newly born stars radiate intense ultraviolet (UV) photons which govern the chemical and the physical properties of the nearby molecular clouds. The molecular clouds, of course, consist mostly of molecular hydrogens (H_2). The observations of molecular clouds, however, have been limited to tracing molecules, *e.g.*, CO, CS, and HCN. Since hydrogen is the lightest atom, the moment of inertia of H_2 is very small, and the lowest energy levels of H_2 have excitation temperatures that are too high (*e.g.*, $\Delta E/k \approx 500$ K for $J = 0 \rightarrow 2$) to be thermally excited in the cold ($T_{\rm gas} < 50$ K) molecular clouds. Also, H_2 is a homonuclear molecule for which dipole transitions in the vibration-rotation states are prohibited and only the quadrupole transitions are allowed. Recently, the Far Ultraviolet Spectroscopic Explorer (FUSE) has observed H_2 absorption bands from translucent molecular clouds with their background stars [1–4].

Extreme-UV photons whose energies are bigger than the Lyman limit ($E_{\rm photon} > 13.6$ eV) are absorbed in the HII regions, and the far-UV photons (6 eV $< E_{\rm photon} <$ 13.6 eV) penetrate the surfaces of nearby molecular clouds until they are absorbed by dust, H_2, C, and CO. The absorbing regions, where the far-UV photons dominate the ionization of atoms, the formation and de-

*E-mail: kiseon@kao.re.kr

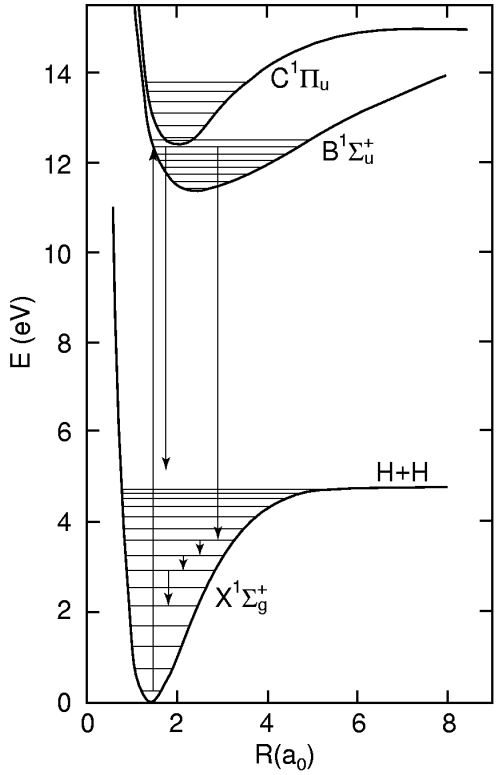

Fig. 1. Energy levels of molecular hydrogen. The transitions between the electronically excited energy levels ($B^1\Sigma_u^+$ and $C^1\Pi^u$) and the electronic ground level ($X^1\Sigma_g^+$) consist of the Lyman-Werner bands in far-UV bands. The transitions within the vibration-rotation energy levels cause the quadrupole transition emission lines in the near- and the mid-IR bands. Also note that the transition probability follows the Franck-Condon principle. This figure is adapted from Fig. 3.1 in Ref. 7.

struction of molecules, and the heating of the gas, are called *photodissociation regions* or *photon-dominated regions* (hereafter, PDRs) [5, 6]. In general, the PDRs include most of the atomic gas in a galaxy, both in diffuse clouds and in the denser regions. We are focusing on the dense ($n > 10^2$ cm^{-3}) regions in this paper.

H_2 molecules which absorb far-UV photons in the Lyman ($B^1\Sigma_u^+ - X^1\Sigma_g^+$) and Werner ($C^1\Pi^u - X^1\Sigma_g^+$) bands are electronically excited (see Fig. 1). Subsequent fluorescence leads to dissociation of the H_2 molecules in about 10 % of the cases and to H_2 molecules in vibrationally excited states of the ground electronic state in the remaining 90 % of the cases [8]. The excited molecules in these vibration-rotation levels then cascade down to the lower vibration-rotation levels on a time scale of 10^6 sec by emitting quadrupole transition lines in the near- and the mid-IR bands [8,9]. The fluorescent emission in the IR bands has been observed in various star-forming regions [10–16].

When the fluorescent transitions from the electronically excited state to the various vibration-rotation states in the electronic ground state occur on the time scale of 10^{-8} sec, far-UV lines in the Lyman and Werner bands are emitted. Since the far-UV band data are only accessible from the space telescope, a few observations of these H_2 emission have been reported, *e.g.*, the reflection/emission nebula IC 63 [17,18], the diffuse interstellar medium [19], the pre-main-sequence star T Tauri and Burnham's nebula [20,21], the Herbig-Haro objects HH 43 and HH 47 [22], and Jupiter's aurora [23,24].

The studies of PDRs are not only to understand the physics and the chemistry of the molecular clouds but also to understand the process of star formation. If the observed emission lines are successfully fitted with the model calculations, we can deduce the populations of the newly born stars near the PDRs [25–28].

The Far-ultraviolet IMaging Spectrograph (FIMS) is the main payload onboard the first Korean scientific satellite, "KAISTSAT-4", which will be launched in 2003 (see Refs 29 and 30 for a general description of the FIMS). The FIMS plans to make an all-sky survey with $3^\circ \times 3^\circ$ pixel resolution and to perform pointing observations afterward with $5' \times 5'$ pixel resolution in the $900 - 1150$ Å and the $1335 - 1750$ Å bands. The primary scientific goal of the FIMS is to measure hot ($T_{\rm gas} = 10^{4.5} - 10^6$ K) plasma in the Galaxy. The observed spectral bands also cover the H_2 Lyman-Werner band emission lines from the PDRs. In this paper, we calculate the expected sensitivity of the FIMS to the H_2 Lyman-Werner band emission and suggest the required observing times for the previously detected PDR sources.

II. SENSITIVITY CALCULATIONS

1. Far-UV Imaging Spectrograph, FIMS

The FIMS optical system consists of two wavelength bands, and each spectrograph channel has a collecting mirror, slit, filter, grating, and detector. Each channel uses identically figured $\sim 5 \times 8$ cm^2 optics, an off-axis parabolic cylinder mirror, and an elliptically figured and holographically ruled grating in the same geometrical configuration. The cylindrical-scanning method provides twice the grasp and field of standard spectrographs, even with fast ($f/2.2$) figure optics [31–33]. Imaging performance is also allowed for a large field with an imaging resolution on a scale of arcmin, similar to those of other important interstellar all-sky surveys. The FIMS is optimized for faint diffuse radiation rather than for point sources; thus, it is ∼10 time more sensitive to the diffuse source than previous missions [34]. The sensitivity for diffuse radiation was compared with those on previous missions in Ref. 34.

Radiometric performances are characterized by the effective grasp, which relates the intensity of emission sources and detector signals (photon counts). The value is derived by multiplying the geometric area, the reflectivity of the optical components, the quantum efficiency

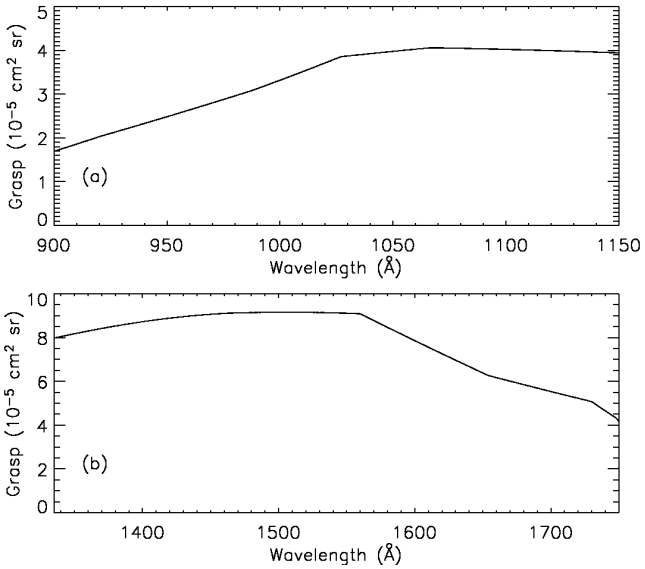

Fig. 2. Grasps for the (a) short- and the (b) long-wavelength bands of the FIMS.

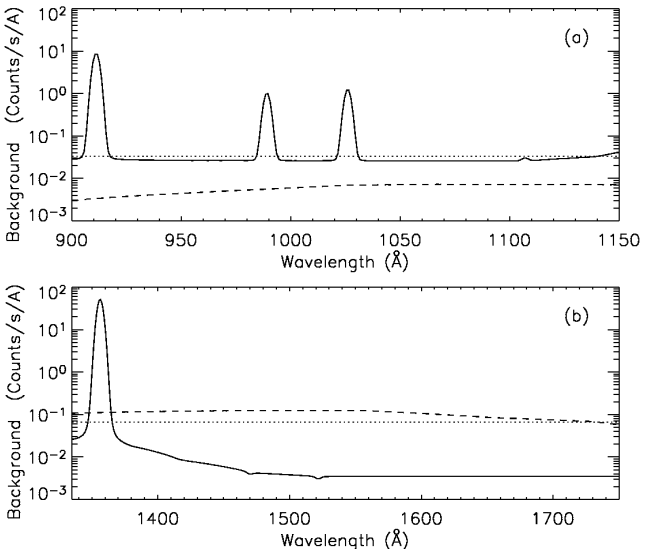

Fig. 3. Backgrounds for the (a) short- and the (b) long-wavelength bands of the FIMS. The solid, the dotted, and the dashed lines represent the backgrounds due to the night airglow, the detector background, and the diffuse cosmic far-UV background radiation, respectively.

of the micro-channel plate (MCP), and the solid angle the detector sees. The values are different for each bands and depend on the physical parameters of the optical components even though their geometrical factors may be identical.

An optical calibration of the flight model of the FIMS was performed by using the EUV calibration facilities at the Space Sciences Laboratory of the University of California, Berkeley to measure the optical parameters, the transmittance of the CaF_2 filter in the short-wavelength band, the reflectivities of the gratings and mirrors, the diffraction efficiencies of the gratings, and the quantum efficiencies of the MCPs [35]. Detailed information on the FIMS calibration will be provided elsewhere. Figure 2 shows the effective grasp values for each band derived from the preliminary results of the FIMS calibration. The figure shows that the grasp values vary up to ~ 50 %, depending on the wavelengths within each band.

Several background emission sources may be obstacles to indisputable identification of the emission lines of the H_2 fluorescence. The dominant background source is the geocoronal emission from the earth's upper atmosphere. The night airglow line intensities in Ref. 36 show that Lyα, Lyβ, and OI emission lines are prominent in the far-UV bands (see references in Ref. 34). Continuum backgrounds, which originate mainly from dust scattering of stellar far-UV radiation, are assumed to be 100 and 500 counts cm^{-2} s^{-1} sr^{-1} Å^{-1} for the short- and the long-wavelength bands, respectively [37]. The detector background of the FIMS flight model was measured, and the background summed over all detector area had a typical value of ~ 2 count s^{-1} in both the short- and the long-wavelength bands. The other important noise source is Lyα scattering, which is significant in the short-wavelength band. Lyα emissions enter into the FIMS wavelength bands via scattering off the grating surfaces. Figure 3 shows the intensities of the various background components summed over the full field of view (FOV) ($4^\circ \times 5'$ and $8^\circ \times 5'$ for the short- and the long-wavelength bands, respectively). The scattered noises of Lyα, as well as of the other airglow lines, were included in the calculation of the airglow backgrounds.

2. Model Spectra of H_2 Fluorescent Emission

Sternberg [38] calculated the far-UV fluorescent H_2 emission spectra produced in cold ($T < 500$ K), isothermal, and low-density ($n \sim 10^4$ cm^{-3}) clouds exposed to external far-UV radiation fields. The input parameters for the model calculations were the total density of hydrogen nuclei (n), the total intensity of the incident far-UV fields (χ), the spectral energy distributions of the incident far-UV fields ($T_{\rm UV}$), the molecular formation rate coefficient (R), and the effective dust UV continuum absorption cross-section (σ). It should be noted that he did not calculate the heating and cooling processes in the PDRs.

The results assumed that the PDR had an isothermal temperature of 100 K with a hydrogen-nuclei density of 10^3 cm^{-3}. The incident far-UV field was 10^2 times the average interstellar UV field ($\chi = 10^2$). The total H_2 intensity of the far-UV emission lines was 1.12×10^{-4} erg s^{-1} cm^{-2} sr^{-1}. Since the table includes only the 260 brightest lines, their summed contribution comprises only 45.6 % of the total radiated power. We, thus, assume that the weaker lines follow the spectral distribu-

tion of the stronger ones and simply scale the tabulated spectrum upward to account for the missing flux, as in Ref. 18. Hereafter, the tabulated model in Ref. 38 will be referred to as the standard model.

The total UV intensity depends on the physical parameters in the PDR, *e.g.*, $T_{\rm gas}$, n, σ, R, and χ, whereas the relative line intensities are sensitive only to very large changes in the spectral shapes of the incident far-UV continua. In the case of $T_{\rm gas} = 500$ K, $n = 10^5$ cm^{-3}, and $\chi = 10^4$, the total UV intensity is 2.2×10^{-2} erg s^{-1} cm^{-2} sr^{-1}, which is about two orders of magnitude larger than it is in the former case.

Recently, Pak *et al.* [39] calculated the H_2 fluorescent spectra by using the radiative transfer code CLOUD [9, 40], in which the efficiency factor of molecular formation on gain surfaces is assumed to be $y_{\rm F} = 3$. They tabulated the total H_2 fluorescent intensities in far-UV for various physical parameters: the hydrogen density, the incident far-UV radiation, and the gas temperature. The total intensity corresponding to $\chi = 100$, $n = 10^3$ cm^{-3}, and $T_{\rm gas} = 100$ K, obtained by interpolation of their tabulated data, is higher than that of Sternberg by a factor of ~ 6. The discrepancy between the two models is mainly due to the adoption of a higher efficiency factor $y_{\rm F}$ and to the inclusion of bound-continuum, as well as bound-bound, emission in Ref. 39. They also included the heating and the cooling processes among the molecules and atoms in the calculation of the PDR models.

Although the code CLOUD is more complicated and rigorous, the overall shapes of the resulting spectra are similar to those of Sternberg, and the previous observations of PDRs have been compared with the predictions of Sternberg's model (see, for example, Ref. 18). Therefore, it would be better to adopt the Sternberg model as the standard model for comparison with previous observations and simply to scale the result upward if required. The Sternberg model was, thus, used throughout the present study.

Figure 4 shows the model spectra based on the model calculation of Sternberg [38] in the short- and the long-wavelength bands of the FIMS. We made these spectra using the tabulated spectrum in Table 2 of Ref. 38. In order to simplify the calculation, typical spectral resolutions of 1.8 Å and 2.7 Å were assumed throughout the short- and the long-wavelength bands, respectively. The count was derived from the line intensity of each source. For the line emissions, the line intensities were convolved with the scattering profile of the grating and a Gaussian with typical half energy widths (HEWs), and the counts of each component were summed up to give the theoretically expected total count for each bin. The resolution referred to in the present paper is the HEW, which is related to the standard deviation of Gaussian function by HEW $= 1.35\sigma$. As for the source geometry, we assumed throughout the present study that the PDR source filled one pixel ($5' \times 5'$) of the FIMS FOV.

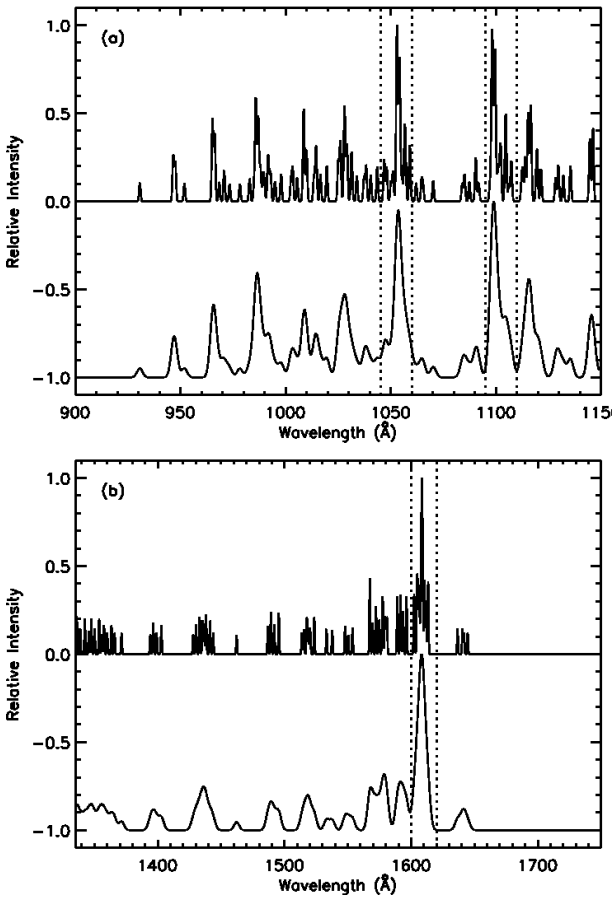

Fig. 4. H_2 emission spectra calculated using the model of Sternberg [38]. The upper plot is for the short-wavelength band of the FIMS, and the lower plot is for the long-wavelength band. The upper spectra (thin lines) were calculated for a spectral resolution of 0.5 Å, and the lower spectra (thick lines) for 1.8 Å and 2.7 Å, which are the typical spectral resolutions of the FIMS in two bands. The lower spectra have the theoretically expected shapes of blended lines when observed with the FIMS. Also shown are dotted vertical lines which represent the spectral bands selected for the detectability test with the FIMS.

3. Exposure Map of the All-sky Survey

An all-sky survey exposure map is obtained using a simple analytic calculation. The FIMS will make an all-sky survey by scanning the entire sky along the short axis of the slit, *i.e.*, along the $5'$ field direction of the $8^\circ \times 5'$ FOV. In each orbit, the FIMS FOV scans 180°, from an ecliptic pole to the opposite ecliptic pole, during the eclipse time ($\sim$ 25 min), and the pole-to-pole scanning drifts 360° along the ecliptic equator for one year because of the properties of a sun-synchronous orbit (see Fig. 5, and Fig. 1 in Ref. 41). A line of site in the ecliptic equator will be observed during the time that the $5'$ field is crossed, and the line of site will be crossed several times due to the FOV drift along the ecliptic equator. The

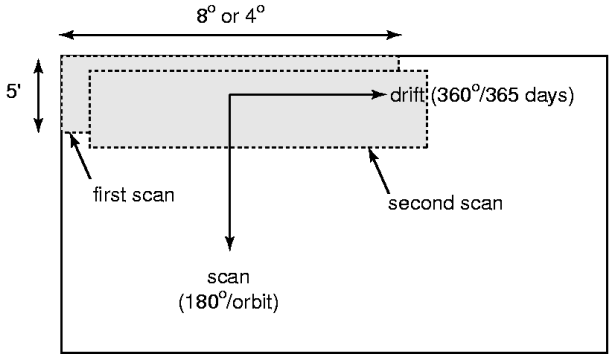

Fig. 5. Schematic diagram of the all-sky survey.

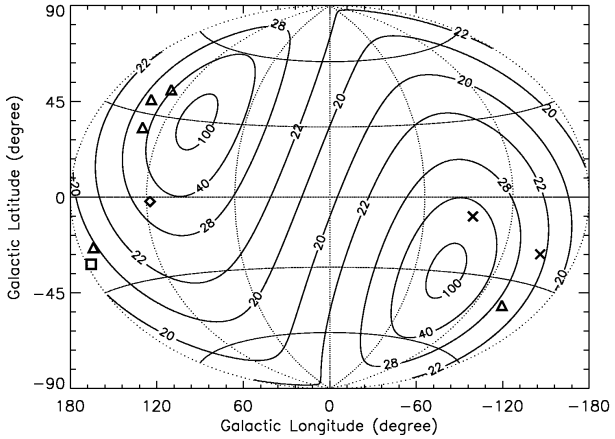

Fig. 6. The aitoff projection of the all-sky survey exposure map for the short-wavelength band of the FIMS. The contour levels are in units of sec. The exposure map for the long-wavelength band may be obtained by scaling the exposure times upward by a factor of 2. The diamond, the triangles, the squares, and the crosses represent the locations of the reflection nebula IC 63 [18], of the five molecular clouds detected by Martin *et al.* [19], of T Tauri and Burham's nebula [21], and of two Herbig halo objects, HH 43 and HH 47 [22], respectively.

exposure time for the line of site in the ecliptic equator is, then, given by multiplying the time crossing $5'$ and the total number of crosses due to the FOV drift. The total number of crosses for the line of site is obtained by multiplying the number of orbits assigned to the sky survey observation in a day and the number of days in which the 8° field (or 4° field for the short-wavelength band) is fully covered by the drift, *i.e.*, 365 days/360° × 8° (or ×4°).

If 7 orbits a day are assumed for the sky survey observation, the exposure time for a line of site in the ecliptic equatorial plane is ∼38.3 sec for the long-wavelength band and ∼19.2 sec for the short-wavelength band. At an arbitrary ecliptic latitude θ, the circumference of the circle defined by the latitude is $2\pi\cos\theta$; thus, the number of crosses at this latitude is given by multiplying the number at the ecliptic equatorial plane ($\theta = 0$) by a factor of $1/\cos\theta$. The exposure time at the latitude is, then, multiplied by the same factor.

The aitoff projection of the calculated exposure map is shown in Fig. 6, in which the contour map is shown in the Galactic coordinate system. Since the FOV of the long-wavelength band is twice that of the short-wavelength band, the exposure map for the long-wavelength band can be obtained by multiplying by a factor of 2. Also shown in the figure are the locations of previously detected H_2 emission sources. The South Atlantic Anomaly and the moon interrupt continuous operation. A more rigorous calculation of the exposure time considering these effects may be found in Ref. 41.

4. Required Observation Time

The signal-to-noise ratio (SNR) has been used as a standard for the detectability test of a proposed signal. Hernandez *et al.* [42] noted, however, that an "*a-priori*" test of detectability in a future experiment would not be the same as an "*a-posterior*" one deciding whether a real signal had been detected, given an observed signal from a past experiment. They also provided a rather complex algorithm for finding the correct confidence level of detectability for a given theoretical signal value. The SNR should be used only to determine the reliability level of an observed signal from a past experiment. For a rigorous test of the detectability, extensive Monte Carlo simulations must be performed as in Ref. 34.

Assuming that a signal follows a Gaussian distribution, Bityukov and Krasnikov [43] showed that the following formula is a reliable approximation to the "true" significance level of detectability in a newly planned experiment:

$$S = \sqrt{\mu_{\rm S} + \mu_{\rm B}} - \sqrt{\mu_{\rm B}}, \qquad (1)$$

where $\mu_{\rm S}$ and $\mu_{\rm B}$ represent the theoretical mean values of the signal and the background, respectively. Recently, Seon [44] also investigated a detectability test based on the statistical theory of hypothesis testing and found that this formula is applicable not only to a Gaussian distribution but also to a Poisson distribution in spite of an error in the original derivation in Ref. 43.

The observation time required to detect the H_2 emission at a certain confidence level was derived by using Eq. (1) and by assuming the standard model of Sternberg. Figure 7(a) shows the estimated significance levels as functions of the observation time. In the figure, we chose two blended lines, peaked at ∼ 1055 Å and ∼ 1100 Å, in the short-wavelength band and one blended line at ∼ 1607 Å in the long-wavelength, as denoted by dotted vertical lines in Fig. 2, where the H_2 line emission is prominent without blending with the geocoronal emission lines. It can be seen that about 50 seconds of integration is required to reach 3σ detection of the H_2 fluorescence for both wavelength bands.

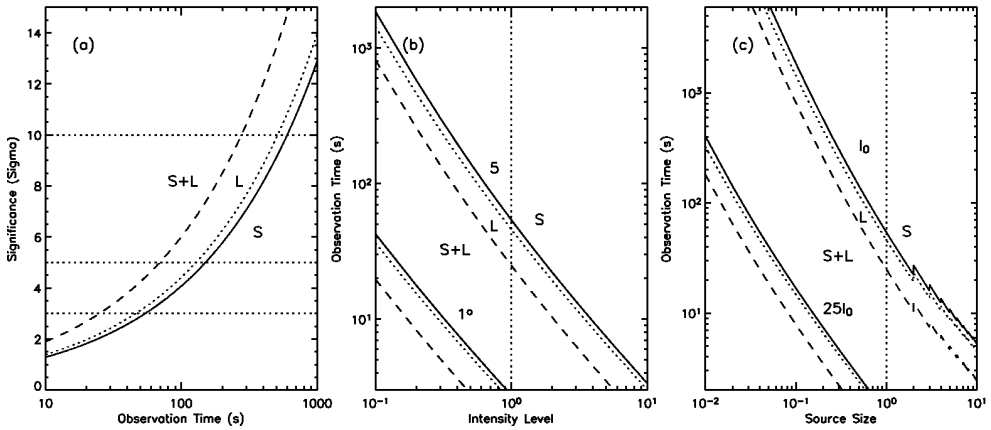

Fig. 7. (a) Detection significance level versus observing time, (b) observation time, required to lead detection at the 3σ confidence level, versus relative intensity to the standard model of Sternberg, and (c) observation time, required to lead detection at the 3σ confidence level, versus source size in units of $5'$. The solid and the dotted lines represent the significance levels of detectability for the short- and the long-wavelength bands, respectively. The strongest blended lines, which peaked at ~ 1055 and ~ 1100 Å and at ~ 1607 Å, were used for the calculation in the short- and the long-wavelength bands, respectively. The dashed lines denote the values obtained by combining all three blended lines. The lower three lines in (b) were obtained when the size of the extended source was 12 times bigger than the one-pixel size ($5'$) of the FIMS, and those in (c) were obtained when the intensity was 25 times higher than that of the Sternberg's model (I_0).

Since the total integration time for most lines of site after one-year sky survey is less than 50 seconds in the short-wavelength band, the fluorescent emission of H_2 may not be detected in this wavelength band after the sky survey. Thus, pointing observations are needed to detect the H_2 emission from PDRs in the short-wavelength band.

In the case of the long-wavelength band, we can reach an $\sim 3\sigma$ confidence level for about half of the sky. Moreover, combining all three blended lines in both wavelength bands, the observation time required to reach the 3σ confidence level is only ~ 25 sec; thus, the 3σ level may be achieved for most directions of the sky. In other words, we might find H_2 emissions other than from previously observed sources, provided that there are PDRs where the emission intensity of H_2 is equal to or slightly stronger than the model we have used in the study and provided that the PDRs are sufficiently separated ($\geq 10'$) from very bright stars because the instrument has to be turned off whenever high count rates occur [45].

The total intensity ratios of other blended lines to the reference blended lines with which the required observation times were calculated are $\sim 0.05-0.25$ for the short-wavelength band and $\sim 0.2-0.5$ for the long-wavelength band. The observation times required to obtain some more information are, thus, about 2,000 s (~ 1.4 orbit) for the short-wavelength band, and about 600 s for the long-wavelength band.

III. DISCUSSION

1. Physical Parameters

We have to note that the model is for a PDR with $T_{\rm gas} = 100$ K, $n = 10^3$ cm^{-3}, and $\chi = 10^2$. Even though the relative intensities of the H_2 fluorescent emission lines are sensitive only to the spectral energy distribution of the incident far-UV radiation, the absolute intensity is very sensitive to the physical parameters. The intensities of the fluorescent emission lines in the direction normal to the cloud surface are given approximately as

$$\frac{I(\chi, T_{\rm gas}, n)}{I(\chi_0, T_0, n_0)} \approx 6.9\frac{\chi}{\chi_0}\left[1 + 5.9\frac{\chi/\chi_0}{\sqrt{T_{\rm gas}/T_0}(n/n_0)}\right]^{-1} \quad (2)$$

by using an approximate scaling equation provided by Sternberg [38] and by adopting the typical values of the molecular formation rate coefficient, the unattenuated photodissociation rate, and the effective grain absorption cross-section. Here, the subscript '0' repesent the standard parameters adopted for the standard model. When the temperature ($T_{\rm gas}$) and the gas density (n) are sufficiently high, a fixed fraction of the incident far-UV radiation (χ) is absorbed by the hydrogen molecules rather than by the dust in the cloud, and the intensity of the fluorescent emission lines is proportional to the incident far-UV radiation. On the other hand, when the temperature and the density are low enough, a decreasing fraction of the incident far-UV radiation is absorbed by the molecule, and the total intensity is then independent of the incident radiation.

For the PDRs in the Orion cloud and NGC 2024, the temperature varies from 10 to 300 K, the gas density

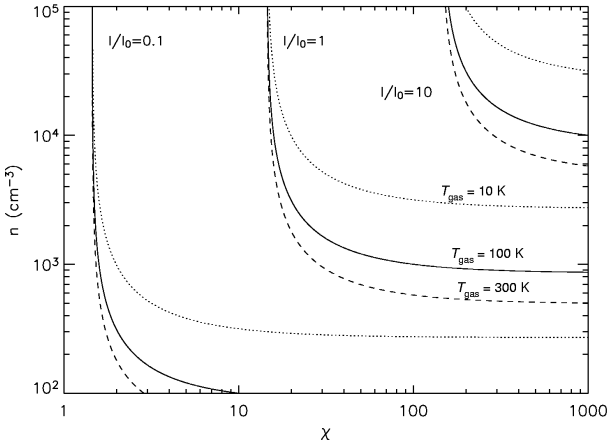

Fig. 8. Contours of constant total H_2 fluorescent intensity for $I/I_0 = 0.1, 1$, and 10. The dotted, the solid, and the dashed lines represent the contours estimated for $T_{\rm gas} = 10, 100$, and 300 K, respectively.

from 10^3 to 10^5 cm^{-3}, and the incident far-UV radiation from 10 to 10^3 [10,13]. If the absolute intensity is 3 times higher than that of the standard model of Sternberg, we can easily get a higher ($> 5\sigma$) significance level with an observing time of a few tens of seconds. Figure 8 shows the dependence of the total intensity of the fluorescent emission lines on the typical values of the physical parameters ($T_{\rm gas}$, n, and χ) of the PDRs in the Orion cloud and NGC 2024. The total intensity is larger than that of the standard model for a large portion of the parameter space shown in Fig. 8. Figure 7(b) shows the observation time required to reach the 3σ confidence level as a function of the intensity relative to the Sternberg's model. It should be noted that the standard model of Sternberg does not include bound-continuum emission, which may increase the detection probability.

2. Source Size

Another important parameter for the sensitivity estimate is the source size of the emission source. Our estimate assumed that the size of the extended source was equal to the one-pixel size of the FIMS ($5' \times 5'$). Figure 7(c) shows the variation of the observation time required to reach the 3σ confidence level with the source size. The figure shows step-wise features because the background signals are incident from the entire source size of $5'$, or its multiples, while the source signals come from an arbitrary source size. For the same reason, the background intensity from the entire $5'$ pixel was accounted for even when the source size was less than $5'$.

For the reflection/emission nebula, IC 63, the total H_2 emission intensity in the far-UV bands is 2.8×10^{-3} erg s^{-1} cm^{-2} sr^{-1}, which is about 25 times higher than that of the standard model [38]. The size of IC 63 is $\sim 40''$ in diameter [18,46]. However, this value may be underestimated. From the HII region picture of IC 63 in the blue *Palomar Observatory Sky Survey* plate (see Fig. 1 in Ref. 17), we found that the source size might be $\sim 0.5'$. The required observation time for an intensity 25 times higher than that of the Sternberg model is shown in the lower three lines of Fig. 7(c). For a source size of $\sim 0.5'$, the required observation time is only $\sim 10 - 20$ sec for IC 63; thus, the source can be observed by the all-sky survey.

Table 1. Required observation time for all molecular clouds previously observed in the far-UV[a].

Name	l	b	$I_{\rm tot}/I_0$	F	$T_{\rm obs.}$
IC 63	117	–1.6	25	0.1	7.9 s
Target 2	132	40	1.2	12	63 s
Taurus cloud	168	–16	2.1	12	26 s
Lindblad complex	135	25	2.3	12	23 s
Ursa Major cloud	142	35	1.2	12	67 s
Target 7	216	–39	0.8	12	136 s

[a]Note – The required observation time is the time to reach the 3σ confidence level with combined signals of three blended lines. l and b are the galactic latitude and longitude, respectively. I_0 is the total intensity of the standard model of Sternberg [38], 6.87×10^6 photons cm^{-2} s^{-1} sr^{-1}. See Ref. 18 for IC 63 and Ref. 19 for the other clouds. The names of Targets 2 and 7 in Ref. 19 are not known.

On the other hand, some PDRs in our Galaxy are very extended. Luhman and Jaffe [11] observed the Orion A molecular cloud in the H_2 $v = 1 \rightarrow 0$ S(1) emission line ($\lambda = 2.1218$ μm) and found that the PDRs were extended up to 2°. If we add all the fluxes in the 2° slit length (or in 24 pixels), the sensitivity can be improved by a factor of $\sqrt{24}$. Figure 7(b) also shows the required observation time for an extended source a 12 times the FIMS pixel size, *e.g.*, with a size of 1°. In Table 1, we show the required observation times for the six previously observed molecular clouds reported in Refs. 17-19. Here, we estimated the total intensities of the clouds from the intensities of the Lyman band emissions tabulated in Ref. 19, and we assumed a size of 1° for the clouds.

At this point, it should be noted that the observation times in Table 1 were estimated for the case the FIMS FOV was fixed toward a specific line of site in the sky and, thus, for a pointing observation. When sky survey data are considered, the source signals acquired for an extended source larger than a pixel of the FIMS can, thus, be added along the scan direction, which is perpendicular to the long axis of the slit, and along the long axis. This has the effect of increasing the total intensities to 12 times higher than those listed in Table 1 and of making the exposure time required in a sky survey less than 10 sec. These clouds can, thus, be detected with an all-sky survey.

We might observe star-forming molecular clouds in external galaxies, *e.g.*, the Large Magellanic Cloud. Pak *et al.* [10] observed near-IR H_2 emission lines from the 30

Doradus region in the Large Magellanic Cloud and estimated a density of 10^4 cm^{-3} and an incident far-UV intensity of $\chi \sim 10^{2.7}$. Pak *et al.* [10] also found that the PDR was extended up to $\sim 3'$. A H_2 absorption study with FUSE shows that the H_2 temperature is $\sim 50-100$ K [1–4]. When these parameters are used, the expected intensity of the H_2 fluorescent emission is ~ 6.7 times larger than the total intensity of the standard model. If the source size is $\sim 3'$, H_2 emission may be detected with only an observing time of ∼40 s for the short-wavelength band.

IV. CONCLUSIONS

We used the PDR model by Sternberg [38] in order to estimate the observing time of the FIMS for detecting H_2 fluorescent emission lines. Sternberg's [38] calculations, however, are limited to only a few physical cases, so we could not precisely estimate the required observing time. Detailed calculations for the PDR models are required to more accurately predict fluxes and to analyze the observational data.

Our results show that the FIMS can detect, when all the peaked emission lines are added, H_2 fluorescent emissions from the previously observed PDRs with one-year survey observation. More detailed spectral information can also be obtained with a pointed observation of about ~ 2 orbits, corresponding to about a 3,000-s observation.

In contrast to the previous missions optimized for point sources, the FIMS is optimized for faint diffuse radiation and is ∼10 times more sensitive to the diffuse radiation than FUSE [34]. With its high sensitivity to diffuse radition, the FIMS may detect more H_2 fluorescent emissions, which were not observed previously.

ACKNOWLEDGMENTS

This work was financially supported by the Astro21 program of Korea Astronomy Observatory, and KAISTSAT-4 program and the BK21 Project of the Korean Government. The authors would like to thank an anonymous referee for suggestions that improved the manuscript significantly.

REFERENCES

[1] B. L. Rachford, T. P. Snow, J. Tumlinson, J. M. Shull, W. P. Blair, R. Ferlet, S. D. Friedman, C. Gry, E. B. Jenkins, D. C. Morton, B. D. Savage, P. Sonnentrucker, A. Vidal-Madjar, D. E. Welty and D. G. York, Astrophys. J. **577**, 221 (2002).

[2] J. M. Shull, J. Tumlinson, E. B. Jenkins, H. W. Moos, B. L. Rachford, B. D. Savage, K. R. Sembach, T. P. Snow, G. Sonneborn and D. G. York, Astrophys. J. Lett. **538**, 73 (2000).

[3] T. P. Snow, B. L. Rachford, J. Tumlinson, J. M. Shull, D. E. Welty, W. P. Blair, R. Ferlet, S. D. Friedman, C. Gry and E. B. Jenkins, Astrophys. J. Lett. **538**, 65 (2000).

[4] J. Tumlinson, M. J. Shull, B. L. Rachford, M. K. Browning, T. P. Snow, A. W. Fullerton, E. B. Jenkins, B. D. Savage, P. A. Crowther, H. W. Moos, K. R. Sembach, G. Sonneborn and D. G. York, Astrophys. J. **566**, 857 (2002).

[5] A. G. G. M. Tielens and D. J. Hollenbach, Astrophys. J. **291**, 722 (1985).

[6] D. J. Hollenbach and A. G. G. M. Tielens, Rev. Mod. Phys. **71**, 173 (1999).

[7] E. F. van Dishoeck, *Molecular Astrophysics* (Cambridge Univ. Press, New York, 1990), p. 59.

[8] J. H. Black and A. Dalgarno, Astrophys. J. **203**, 132 (1976).

[9] J. H. Black and E. F. van Dishoeck, Astrophys. J. **322**, 412 (1987).

[10] S. Pak, D. T. Jaffe, E. F. van Dishoeck, L. E. B. Johansson, and R. S. Booth, Astrophys. J. **498**, 735 (1998).

[11] M. L. Luhman and D. T. Jaffe, Astrophys. J. **463**, 191 (1996).

[12] M. L. Luhman, D. T. Jaffe, L. D. Keller and S. Pak, Astrophys. J. Lett. **436**, 185 (1994).

[13] M. L. Luhman, D. T. Jaffe, A. Sternberg, F. Herrmann, and A. Poglitsch, Astrophys. J. **482**, 298 (1997).

[14] S. Pak, D. T. Jaffe and L. D. Keller, Astrophys. J. Lett. **457**, 43 (1996).

[15] S. Pak, D. T. Jaffe and L. D. Keller, *4th ESO/CTIO Workshop, The Galactic Center*, edited by R. Gredel (Astronomical Society of the Pacific, Tempe, Arizona, 1996), Vol. 102, p. 28.

[16] C. W. Engelbarcht, M. J. Rieke, G. H. Rieke, D. M. Kelly, and J. M. Achtermann, Astrophys. J. **505**, 639 (1998).

[17] A. N. Witt, T. P. Stecher, T. A. Boroson and R. C. Bohlin Astrophys. J. Lett. **336**, 21 (1989).

[18] M. Hurwitz, Astrophys. J. Lett. **500**, 67 (1998).

[19] C. Martin, M. Hurwitz and S. Bowyer, Astrophys. J. **354**, 220 (1990).

[20] A. Brown, M. C. de M. Ferraz and C. Jordan, Mon. Not. Roy. Astron. Soc. **207**, 831 (1984).

[21] A. Brown, C. Jordan, T. J. Millar, P. Gondhalekar and R. Wilson, Nature **290**, 34 (1981).

[22] K. H. Böhm, D. M. Scott and J. Solf, Astrophys. J. **371**, 248 (1991).

[23] Y. H. Kim, J. J. Caldwell and J. L. Fox, Astrophys. J. **447**, 906 (1995).

[24] Y. H. Kim, J. L. Fox and J. J. Caldwell, Icarus **128**, 189 (1997).

[25] C. F. McKee, Astrophys. J. **345**, 782 (1989).

[26] F. Bertoldi and C. F. McKee, *Amazing Light: A Volume Dedicated to C. H. Townes on His 80th Birthday* (Springer, New York, 1996).

[27] H-K. Lee and H-K. Kim, J. Korean Phys. Soc. **40**, 524 (2002).

[28] S. Bastrukov and J. Yang, J. Korean Phys. Soc. **38**, L631 (2001).

[29] J. Edelstein, E. J. Korpela, B. Y. Welsh, K-W. Min, W.

Han, and U-W. Nam, Proc. SPIE **4854**, 329 (2003).
[30] E. J. Korpela, J. Edelstein, P. Berg, M. Bowen, R. Chung, M. Feuerstein, W. Han, J. S. Hull, H. Jin, D-H. Lee, K-W. Min, U-W. Nam, K. Nishikida, J-G. Rhee, K-S. Ryu, K-I. Seon, B. Y. Welsh and I-S. Yuk, Proc. SPIE **4854**, 665 (2003).
[31] K-S. Ryu, K-I. Seon, K-W. Min and J. Edelstein, J. Astron. Space Sci. **15**, 359 (1998).
[32] K-S. Ryu, K. Nishikida, J. Edelstein, K-I. Seon, I-S. Yuk, K. Min, W. Han, E. Korpela, R. Chung and K. McKee, Proc. SPIE **4854**, 457 (2003).
[33] K-I. Seon, K-S. Ryu, E. Korpela, I-S. Yuk, U-W. Nam, W. Han, J-H. Seon, K-W. Min and J. Edelstein, *Proc. 2nd International Conference on Optical Design and Fabrication (ODF2000)* (2000), p. 137.
[34] K-I. Seon, K-S. Ryu, I-S. Yuk, J-H. Park, U-W. Nam, W. Han, J-H. Seon, K-W. Min, J. Edelstein and E. J. Korpela, J. Astron. Space Sci. **17**, 77 (2000).
[35] B. Welsh, J. V. Vallerga, P. Jelinsky, P. W. Veddar, S. Bowyer and R. F. Malina, Opt. Eng. **29**, 752 (1990).
[36] S. Chakrabarti, F. Paresce and S. Bowyer, J. Geophys. Res. **89**, 5660 (1984).
[37] S. Bowyer, Ann. Rev. Astron. & Astrophys. **29**, 59 (1991).
[38] A. Sternberg, Astrophys. J. **347**, 863 (1989).
[39] S. Pak, U. Yu, D-H. Lee, K-W. Min and E. F. van Dishoeck, J. Korean Phys. Soc. **42**, S88 (2003).
[40] C. Sosin, E. F. van Dishoeck and J. H. Black, unpublished reports (1990).
[41] J-H. Park, K-I. Seon, K-S. Ryu, I-S. Yuk, H. Jin, D-H. Lee, S-H. Oh, J. Seon, U-W. Nam, W. Han, W-B. Lee, K-W. Min, J. Edelstein and E. J. Korpela, J. Astron. Space Sci. **18**, 209 (2001).
[42] S. L. Hernandez, S. Navas and P. Rebecchi, Nucl. Instr. Meth. A **378**, 301 (1996).
[43] S. I. Bityukov and N. V. Krasnikov, Mod. Phys. Lett. A **13**, 3235 (1999).
[44] K.-I. Seon, in preparation (2003).
[45] E. J. Korpela and J. Edelstein, internal memo, unpublished (1999).
[46] M. L. Luhman, K. L. Luhman, T. Benedict, D. T. Jaffe and J. Fischer, Astrophys. J. Lett. **480**, 133 (1997).